An innovative tool for measuring sunlight propagation through different snowpacks

Luca Teruzzi[1], Andrea Spolaor[2], David Cappelletti[3], Claudio Artoni[4], Marco A.C. Potenza[1]

5   [1] Department of Physics, University of Milan, Milan, 20133, Italy
   [2] Institute of Polar Sciences, ISP-CNR, Venice, 30172, Italy
   [3] Department of Chemistry, Biology and Biotechnology, University of Perugia, Perugia, 06123, Italy
   [4] Department of Earth and Environmental Sciences, University of Milano-Bicocca, Milan, 20126, Italy

10   *Correspondence to*: Luca Teruzzi (luca.teruzzi@unimi.it)

Abstract. Sunlight penetration in the snowpack plays a fundamental role in many environmental processes, including the local radiative energy balance, snow hydrology and snow microbiology and can potentially contribute to climate change. In addition, many photochemical reactions typically occur in the snowpack driven by solar radiation. Although a few measurements have been attempted in the past decades with several approaches, light penetration through the snowpack is currently almost only

15   modelled numerically, frequently using severe assumptions and several parameters not always easy to be fixed. The lack of experimental data and dedicated studies leave a remarkable scientific gap in the snow research. In this paper, we propose a novel sensor, specifically designed and custom-made, to assess sunlight propagation through the snowpack in three different spectral bands. The probe has been designed to be very compact and lightweight and therefore easily transportable. We measure at different depths in the snowpack the scattered light propagating horizontally with respect to the surface with high spatial

20   resolution (3 mm). Measurements were performed over the past two years across multiple sites with different altitudes and geographic exposure, different illumination conditions and snowpack characteristics. Data are compared to numerical simulations from the "Snow, Ice and Aerosol Radiative" (SNICAR) code, exploited here to extract the information about the light propagation at different depths. This approach provides important constraints to properly model the snowpack characteristics, allowing us to extrapolate this information to the UV radiation range. Nevertheless, in some cases the

25   comparison between our measurement and model run suggest a more complex light penetration depending on the snowpack peculiar characteristics that SNICAR numerical simulations cannot capture. We believe that our tight experimental approach will strongly contribute to a better understanding of the radiative transfer process inside the snow layers, as well as to a quantitative description of all those chemical, physical and biological processes that occur in the uppermost layers of the snowpack.

1 Introduction

Snowpack is a key component in the Arctic regions, in constant evolution and affected by climate condition changes. Fresh snow has a very high albedo, eventually reduced upon aging of snow crystals due to metamorphism and to the presence of impurities, mainly mineral dust and black carbon. Snow light absorption increases with time and with the impurity concentration thus accelerating the melting process. The unique characteristics of light transmission through a snowpack

35 captivate interest across various applications, such as snow albedo and energy transfer to glacier body (Marks et al., 2014), snow hydrology and snow remote sensing (Seidel et al., 2011), ecology (Robson et al., 2019) and lastly snow photochemistry (Spolaor et al., 2019).

The high reflectivity of snow has a significant impact on the distribution of solar radiation at the surface, where even minor changes in reflectivity can result in substantial fluctuations in absorbed radiation. Snow permits some sunlight to penetrate

40 through it. The transmission of light through snow is pivotal in its energy balance, particularly during melting periods, as its optical properties are influenced by the presence of liquid water content (LWC). Liquid meltwater diminishes reflectivity, hastening the melting process and initiating a positive feedback loop (Green et al., 2002; Schlumpf et al., 2024). Light transmission is determined by scattering and absorption, which rely on a combination of snow characteristics and illumination conditions as well as to the different optically distinct layers, such as surface hoar and ice lenses. Optically active particles

45 such as dust and black carbon (aside from air pockets) in the snowpack can significantly diminish both visible and near-infrared reflectance and transmission (Järvinen et al., 2013). An increase of light absorption connected to a change in the light penetration can be translated, in a simplistic way, into an increased capability of the snowpack to absorb energy with a consequent increase of snow melting, and in case the snowpack is above a glacier body, with direct effect on the glacier energy budget (Obleitner et al, 2000; Lackner et al., 2022). Especially in cold climates, the winter snowpack is generally viewed as

50 advantageous for the plants. By thermally insulating the ground, the snowpack helps buffer fluctuations in air temperature and partially reduces solar radiation through reflection and scattering by snowflakes. The fraction of the solar radiation that is not reflected is either absorbed by or passed through the snowpack. This transmitted radiation is accessible to snow algae and plants nestled within the snowpack, facilitating photosynthesis, and conveys environmental information to organisms. Change in light penetration in the snow can affect irradiance and its spectral composition that the plants under the snowpack can receive

55 and use as cues for the timing of phenology. Satellite-based remote sensing harnesses the interaction between light and the snowpack for various applications. The distinctive and spectrally diverse reflectance of snow compared to other typical Earth surface materials serves as the foundation for mapping snow-covered areas. Improving our knowledge on the interaction of light with the snow surface can augment the utility and effectiveness of tools derived from satellite remote sensing. This improvement extends beyond assessing snow cover area to include other physical characteristics of snow, such as snow water

60 equivalent (SWE) (Ma et al., 2023).

In the realm of snow photochemistry research, it is crucial to extract light intensity and flux distributions within the snowpack. In the past, the high latitude snowpack was considered to be chemically inactive because of low temperatures, acting as a giant

cold trap for atmospheric chemical species. However, specific studies and experiments performed in the last decades have demonstrated that the polar snowpacks are photochemically active during the sunlit period, with oxidant concentrations

65 approaching those of tropical or urban mid-latitude environments. Snow represents a highly photochemically active substrate, where photolyzed snowpack impurities can be released as reactive gases in the boundary layer (Raso et al., 2017). When reaching the snowpack, UV radiation can rapidly break weak chemical bonds and, due to its high energy, can promote photochemical reactions, especially in the UV-A (320–400 nm) and UV-B (290–320 nm) wavelength bands (Grannas et al., 2007). For example, mercury in its oxidized forms, mainly as Hg (II), can be deposited onto the snowpack, increasing total

70 Hg concentrations in the upper snow strata. Hg is very labile in the snowpack; it can be reduced back to Hg(0) by the incoming UV radiation and undergo dynamic exchanges with the atmosphere above (Spolaor et al., 2018). Given this, it becomes relatively evident that snow is not merely a final repository for chemical species. Instead, the snowpack has the potential to catalyse chemical reactions under sunlight (Kim et al., 2023), thereby playing a non-negligible role in the geochemical cycle of various elements and compounds.

75 Recognizing the significance of accurately predicting light penetration into snowpacks is crucial, especially when assessing the potential impact on the previously mentioned items. Despite the relatively limited penetration of light into the snow, known as the photic zone, which is confined to the upper snow layer (10 to 15 cm), numerous uncertainties and assumptions persist. While the impact of the uncertainties in estimating the snow photochemical zone at an individual location may appear minor, when applied to the entire Arctic or Antarctic regions, as well as in all the snow-covered areas, the cumulative effect becomes

80 substantial (Robledano et al., 2023). Different approaches are available to estimate the light propagation and interaction with the snow. An extended literature exists for numerical approaches based upon well-established solutions of radiative transfer equation (Flanner et al., 2021; Kokhanovsky, 2022; Whicker et al., 2022) or even dedicated simulations modelling the propagation of light through specific structures within the snow (Zhou et al., 2003; Libois et al., 2013). On the other hand, a uniform approach is still missing for measurements.

85 In the past decades a few measurements have been attempted exploiting several approaches usually based on spectral measurements of both reflected and transmitted sunlight (Beaglehole et al., 1998; Gerland et al., 2000; Hamre et al., 2004; Meirold-Mautner et al., 2004; Warren et al., 2006; Perovich, 2007; Jarvien et al., 2011; Cooper et al., 2021). In many cases, however, these methods are time-consuming, difficult to replicate or characterized by appreciable limitations. For example, in (Beaglehole et al., 1998) the transmitted radiation was measured by extracting from the snowpack a cylindrical volume of

90 about 50 L, large enough to prevent the walls to influence the downward flux. Put on a perforated bench, it was analysed through a silicon detector from below. Similarly, in (Meirold-Mautner et al., 2004) a 2 m high tunnel was dug at a depth of 3.5 m below the snowpack surface. A broadband sensor was inserted vertically upward facing the surface. A different approach was proposed by (Perovich, 2007), where a spectroradiometer was placed directly on the ground before a snowfall to make measurements without disturbing the snow. More recently, in (Jarvien et al., 2011; Cooper et al., 2021) spectral measurements

95 were performed by inserting a spectrometer to record the downwelling flux from horizontal tunnels dug at different depths in the snowpack. A typical limitation is due to the environmental conditions: temperatures are appreciably below zero, the

instrumentation must be properly insulated/heated and can typically operate for relatively short times. Moreover, data interpretation unavoidably depends upon additional information about the parameters that affect the light penetration: ice crystal shape, presence of liquid water, light absorbing particles, algae, etc (Hamre et al., 2004; Meirold-Mautner et al., 2004).

100   Therefore, data interpretation is not model independent (Pedersen et al., 2005; Varsa et al., 2021; Kokhanovsky, 2021). Finally, radiation measurements in the uppermost snow layers (4-7 cm) are either completely discarded from the subsequent data analyses (Tuzet et al., 2019) or modelled by adding further parameters (Cooper et al., 2021). Such a choice is due to the complex, non-diffusive behaviour exhibited by sunlight just below the snow surface. The lack of detailed analyses in the very first centimetres of the snowpack still represents a remarkable scientific gap.

105   Here we propose a different approach by exploiting a new probe specifically designed to measure the sunlight flux in different spectral bands as a function of depth in the upper few centimetres of the ground and sea ice (Mundy et al., 2007; Verin et al., 2022) snowpack. The ultimate aim is to better understand the light-snow interactions under different snowpack conditions and contamination levels. The probe has been carefully calibrated under controlled laboratory conditions and exploited in representative cases. An advantage of our probe is to work in pristine snowpack, without the need for trenching, thus preserving

110   the natural propagation of light. The probe is light and easily transportable, highly resistant and stable. Measurements are easily performed with high spatial resolution (3 mm) even in stratified snowpacks, also with ice lenses and slabs. Thanks to the compact and robust design, the probe can break through crusts up to a few millimetres thick. Examples of the sensibility of experimental results upon different snowpack conditions are reported and data compared to numerical results. In some cases, measurements show specific features that are difficult to be modelled, opening the need of more insights into the light

115   propagation in some peculiar conditions.

We point out that the probe is sensible to visible light: no infrared is detected. As it is well known, visible light propagation through the snowpack is mainly influenced by dust and pollutants (Tuzet et al., 2019), while infrared is sensible to snow structures (Dominé et al., 2006; Langlois et al., 2010). Nevertheless, it is a goal of this approach to analyse the photic zone, irrespectively of dust or pollution. We also work very close to the relevant UV window, where we can extrapolate our results

120   once constrained the light behaviour in the visible.

Moreover, by comparing data to the results of the state-of-the-art, thorough simulation code Snow, Ice and Aerosol Radiative (SNICAR) (Flanner et al., 2021; Whicker et al., 2022), here exploited to recover the light intensities at different depths, we constrain the main features of the snowpack. The corresponding model which best fits data enables us to extrapolate to the UV radiation band in the uppermost layers of the snowpack upon a robust basis. This combined approach addresses the huge

125   challenges associated with directly measuring UV radiation in the snowpack. Although not being a direct measurement, this extrapolation will definitely be close to the real case thanks to the rigorous measurements in the close visible band.

2 Methods

2.1 The light penetration probe

The light penetration probe has been realized to be simple and robust to operate reliably in the environment even under extreme
conditions. Light enters through a small optical window in the head penetrating the snow (see Fig. 1), is totally reflected by a
prism (P) into the color separating prism (CSP) that delivers the red (R), green (G) and blue (B) components onto three
photodiodes (P_R, P_G, P_B). The CSP, provided by OPTEC SpA, is an ensemble of three prisms specifically developed to separate
visible light into three components. The circular entrance diaphragm (area $S = 6$ mm^2), the photodiode surfaces (area $A = 20$
mm^2) and their mutual distance ($L = 50$ mm) define the collection geometrical factor, $SA/L^2 = 0.048$ mm^2 sr and the subtended
maximum angle around 1/10 rad. Figure 1 (a) shows a picture of the probe head with the inner components arrangement. In
Fig. 1 (b) a picture of the probe mounted on the handling stick is reported. The circular entrance diaphragm is shown and the
graded scale (10 mm step) engraved on the outside of the probe is clearly visible. Figure 1 (c) defines the geometry adopted
during the measurements: ϑ_0 is the solar Zenith angle and the probe entrance window is oriented 90° with respect to the Sun
incoming direction.

(a)   (b)   (c)
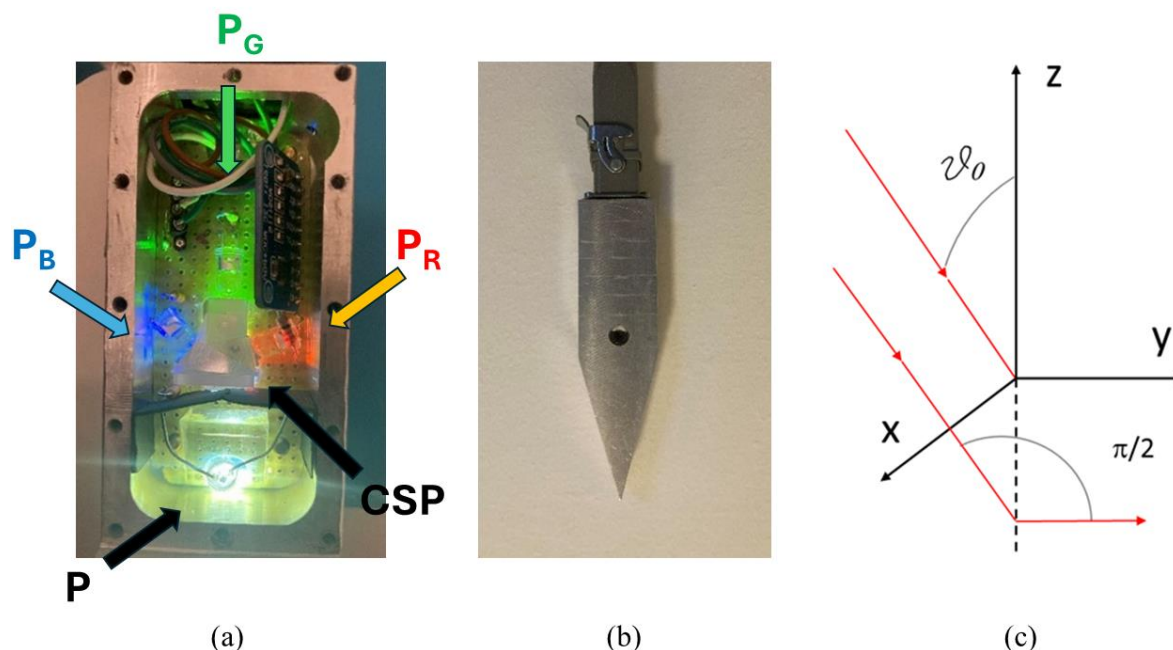
**Figure 1: (a) Picture of the inner part of the probe taken from above, with a white LED delivering light through the window (on the
opposite side of the picture): the CSP separates the light into the R, G, B, components that are then collected by three photodiodes
P_R, P_G, P_B (A = 20 mm^2). All the internal diaphragms to prevent stray light and crosstalk of the three channels have been removed
for taking the picture. (b) the probe (14 x 4 x 4 cm^3) mounted onto the stick. The circular entrance diaphragm (S = 6 mm^2) and the
graded scale (10 mm step) engraved on the outside are also visible here. (c) schematic of the geometric conditions adopted during
the measurements. ϑ_0: solar Zenith angle.**

The photocurrent is converted into voltage and digitization is performed by an ADC placed close to the probe head to keep disturbances at minimum. The digitizer used is an ADS1115, a 16 single-ended channels with a multiplexer for measuring four independent channels and configurable gain to cover an extended dynamic range. The I^2C interface allows easily interface with an Arduino microcontroller wired to the probe through the handling stick. The system provides continuous monitoring of

165 any upper/lower saturation of the signals to optimize the ADC gain setting accordingly. Moreover, an optional Bluetooth interface allows to control the system remotely from a tablet. Once the probe is positioned and the gain set, the measurement is triggered and the microcontroller gets 10 acquisitions in one second. An optional automatic set of the ADC gain has also been implemented into the microcontroller, adapting the gain before each measurement. Raw data are automatically stored into a SD card as text files containing the ADC settings and 10 acquisitions for each measurement position.

170 The three photodiodes collect the light diffused by the snow along the same observation direction, perpendicular to the probe vertical axis. During the operations the probe is inserted vertically through the snowpack, as sketched in Fig. 2. The operator always maintains a minimum distance (few tens of centimeters) from the probe by positioning himself behind the entrance diaphragm, ensuring that his shadow does not interfere in any way with the measurement.

175

180

185

(a)   (b)
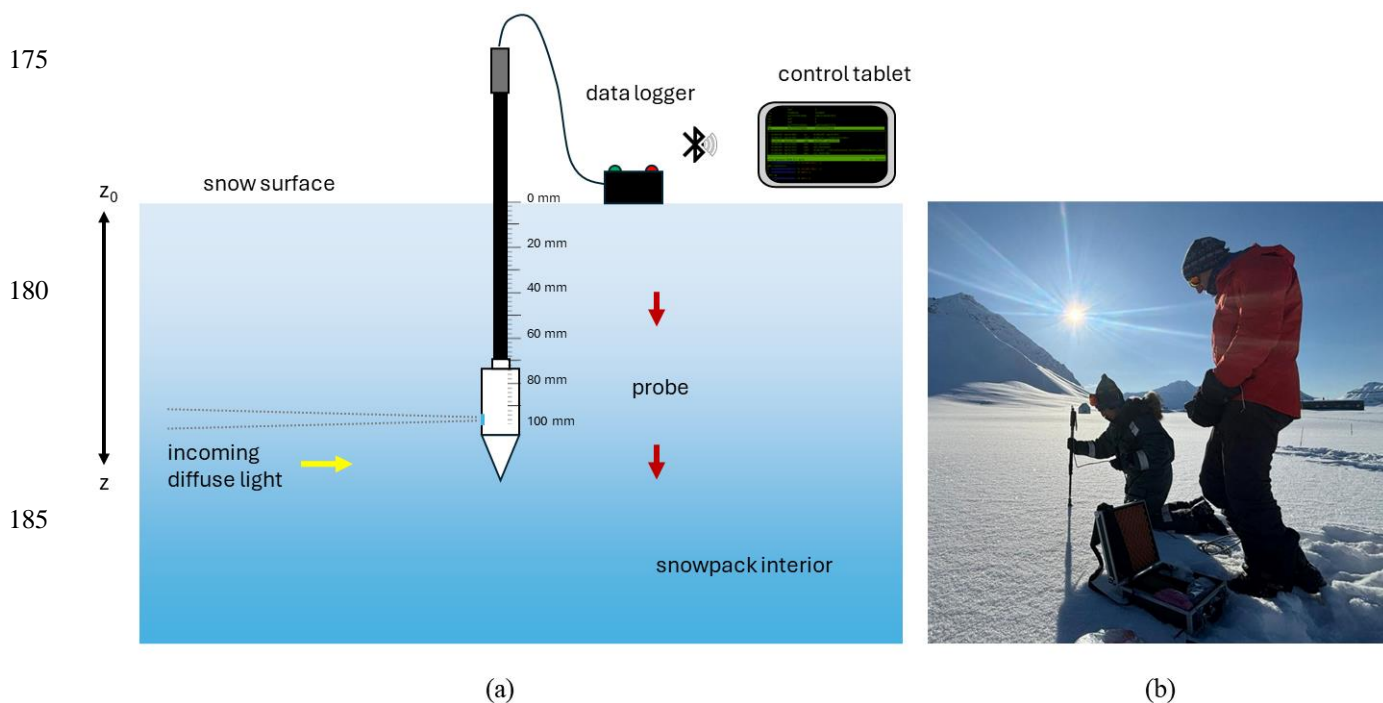
190 **Figure 2: (a) schematic of the measurement procedure with the probe. The probe is inserted vertically with respect to the snow surface (z_0) down to depth z in the snowpack in steps of 10 mm. Signal digitization is performed within the probe, data are stored into the external data logger and Bluetooth connectivity is optionally available to monitor the measurement in real time through a smartphone or tablet. (b) typical probe measuring procedure; the photo was taken close to Ny-Ålesund on 24th March 2023 at ~ 11:00 UTC.**

195   The observation direction is rigorously perpendicular to the vertical plane identified by the Sun and the Zenith directions, therefore $cos\vartheta = 0$ and $\varphi = 0$ (see Fig. 1(c)), where ϑ and φ define the observation and azimuthal angles respectively. Clearly, light enters the probe after complex paths due to multiple scattering events. This geometry introduces some simplification about the data interpretation (see below) and guarantees minimum influence for light propagation in terms of shadows and/or reflections. To limit stray light to affect the measurements the system has proper diaphragms and baffles.

200   Accurate validation of the effectiveness of these items has been obtained by illuminating the entrance window with one color light and checking for the negligible response of the other sensors for all the three colors.

We carefully studied the possible spurious effects introduced by the probe itself to the measurements. These effects might certainly be of utmost importance for deep measurements, when the light flux is small and the light paths are long and complex.

205   To check for the limitations imposed by the probe and to evaluate this potential influence quantitatively, we performed specific laboratory measurements with well controlled granular materials properly illuminated: glass spheres, fine and gross salt grains. Notice that the most important difference of these materials with the true snow, at least in the VIS range, is represented by the absorption, that is always larger for the aforementioned granular media. Since we are interested in characterizing the upper layers, this kind of discrepancies are expected not to be so influent. We compared the results obtained on these analogue

210   systems by operating the probe as we do in the snow to the measurements obtained through an optical fiber with a small glass prism collecting light at 90 degrees, operated from below the sample container (see Fig. A1 in Appendix A). In such a way we introduce no perturbation at all for the light propagation through the granular material above the measurement position and negligible effects at the measurement depth and below. Data have been collected at different wavelengths and compared to those from the probe with no appreciable differences in the upper tens of millimeters (see Fig. A2 in Appendix A).

215   **2.2 Calibration of the light penetration probe under laboratory condition**

The probe has been carefully calibrated in our laboratories at the University of Milan. Moreover, for G light an absolute calibration has also been possible. The head was fixed onto an optical bench, with a white LED moving along a path 1 m long illuminating the entrance window with a light intensity ranging over a dynamic range larger than what measured in the real environment. In Fig. 3 we report the LED spectrum (a) measured through a Hamamatsu spectrometer (Photonic multi-channel

220   analyzer, model C7473-36), the CSP spectral transmission (b) and the responsivity of the photodiode as provided by the company (c). Notice that the large LED-probe distance and the small size of the LED (3 mm side square) guarantee that the light passing through the entrance diaphragm impinges onto a fraction of each sensor surface without any loss, thus allowing to precisely know the illuminating power.

A calibrated power meter (Newport mod. 1815-C, Newport 818-SL) inserted in front of the entrance window provided the

225   reference power for each measurement, then corrected for the additional optical paths to reach each photodiode and for the corresponding collection geometry. The white light power impinging onto the sensors ranged from below 0.05 up to 4 µW approximately, that is wider than the range covered during the field measurements. These values correspond to photocurrents

in the order of µA or fractions, that are converted into voltage and passed to the ADC, operating in the range of tens to hundreds of mV.

230   As it is evident in Fig. 3 (c) and 3 (d), the responsivity can be nicely approximated by a linear behavior and the power spectral density impinging on P_G is almost symmetrical. Therefore, an absolute calibration can be safely performed. On the contrary, the power spectral density in the R band is strongly asymmetric, while the narrow peak in the B band falls in a wavelength range where the responsivity is highly non-linear. Therefore, in both cases we cannot proceed with absolute calibration. Moreover, the sensor responsivity at the wavelengths of the B peak is particularly low, leading to an underestimate overall the

235   B band. Therefore, the B fluxes will be appreciably overestimated.

240

245

250

255

(a)

(b)

(c)

(d)
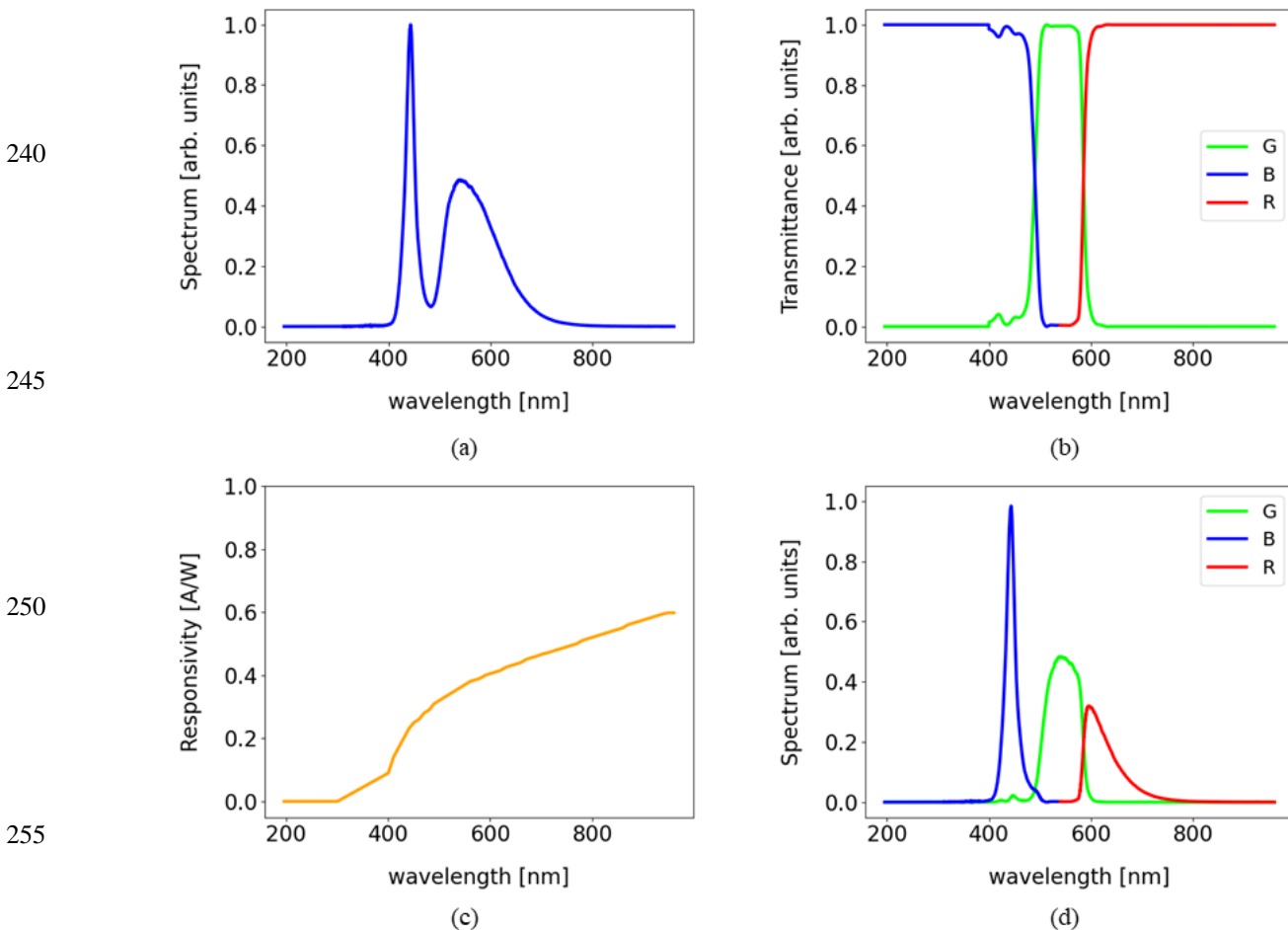
Figure 3: a) Power spectral density of the LED adopted for the calibrations; b) Spectral transmission windows of the CSP, provided by the company; c) Spectral responsivity of the photodiodes, obtained from the data sheet; d) Product of the a), b) and c) curves:

260   **the solid blue, green and red lines describe the spectrum of the light illuminating the P_B, P_G, P_R photodiodes, respectively.**

The calibration curves are linear in the range of interest for all the measurements performed in the real environment, that extend up to readout voltages of less than 230 mV, the maximum in the calibration curves. A very limited influence of the sensor response is then guaranteed.
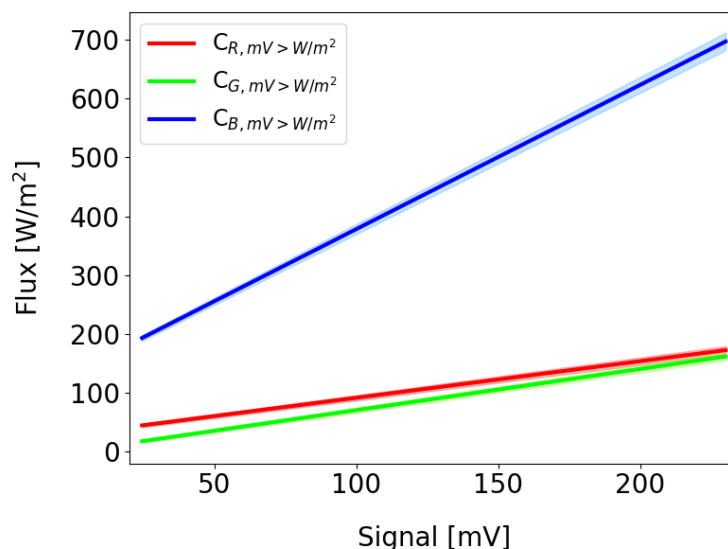
265

Figure 4: Voltage-flux calibration curves retrieved for the R, G and B bands. Abscissas indicate the voltage values (expressed in mV)
280   **measured by the three photodiodes P_R, P_G, and P_B. Ordinates represent the radiation flux [W m^{-2}] calculated by correcting the power measured with the powermeter for the probe collection geometry. The calibration curves show linear behavior over the entire range of interest for our measurements, up to about 230 mV. Uncertainty band (colored shades) are reported as the covariance obtained by linear fitting to data; they are negligible over the whole considered range.**

285   **2.3 Defining the light penetration measurements**

Besides the practical convenience, collecting light propagating in the horizontal direction has advantages in terms of data interpretation, in view of a quantitative evaluation of the physical parameters involved. Light is equally scattered towards the horizontal direction irrespectively of the incoming direction (e.g. either downward or upward). As a drawback of this choice, the measures are not immediately informing about the total light power passing through the snow at a given position, especially
290   in the upper layers where the propagation is not perfectly diffusive.

Following Kokhanovsky (2021), for example, a simple argument can be introduced why measuring light propagating along the horizontal direction is beneficial and simplifies data interpretation. Deep enough where direct sunlight vanishes and light propagation is purely diffusive, the irradiance can be written as a function of the optical depth, τ, and the cosine of the observation angle ϑ, $\mu=\cos\vartheta$ (Eq. (3.70) p. 66 in Kokhanovsky, 2021):

295

$$I(\tau,\mu) = (1 + 3s\mu)\exp{(-k\tau)} \qquad , \tag{1}$$

where $k = \sqrt{3(1-\omega_0)(1-g)}$ is the light diffusion coefficient in snow and $s = (1-\omega_0)/k$ is the so-called similarity parameter, ω_0 is the single scattering albedo, g is the average cosine of the scattering angle, that is the asymmetry parameter

300 for single scattering. Therefore, by introducing the extinction cross section C_{ext} of the single snow grains we can convert the optical depth into geometrical depth z,

$$z = \tau/NC_{ext} \qquad , \tag{2}$$

thus

305

$$I(z,\mu) = (1 + 3s\mu)\exp{(-\gamma\, z)} \qquad , \tag{3}$$

where $\gamma = kNC_{ext}$ gives the inverse characteristic length of the exponential decay (sometimes called asymptotic flux attenuation coefficient, AFEC). It is obtainable from a minimum of two measures of $I(z,\mu)$ performed at two depths, z_1 and z_2, but it is better constrained by a larger number of measurements. The solution $I(z,\mu)$ reduces to its simplest form when $\mu = \cos\vartheta$

310 $= 0$: the pre-factor reduces to identity and the only dependence upon k is in the exponential decay, that is γ. We incidentally note that the radiative transfer equation itself drastically simplifies under these conditions. Measuring along the horizontal direction then provides immediate information about the propagation parameters through the snowpack without any other dependence. In the following, we will fit γ, or better the decay length $1/\gamma$ (sometimes called e-folding depth: see pag. 43 in Kokhanovsky, 2021) by fitting to data collected every 10 millimetres in depth for the light propagating along the horizontal

315 direction.

Modelling the snowpack takes advantage of the possibility of fitting to data from light penetration measurements. To do this, here we exploit the solutions of the Radiative Transfer Equation provided by SNICAR model (Flanner et al., 2007; Cook et al., 2020; Flanner et al., 2021; Whicker et al., 2022) with adding-doubling two-stream solver (Dang et al., 2019; Whicker et al., 2022). SNICAR is a well-accepted approach, usually exploited to recover the spectral albedo of snow. Ultimately, it

320 depends upon the snow features below the surface, that can be carefully imposed into the model.

We also note that in the upper layers a contribution might be relevant from direct light that has not yet been subject to any interaction before being delivered into the probe. Some measurements performed in the past (Beaglehole et al., 1998) suggested similar non-diffusive behaviour. The mathematical description of this case is very difficult and the probability to scatter light

325 into a given direction after the i-th scattering event ultimately depends upon the entire history of the previous scattering events. In view of this potential contribution, exploiting SNICAR for evaluating the light propagation below the surface represents an important help in interpreting data with respect to any model based upon diffusive propagation.

2.4 SNICAR Model description

SNICAR modelling has been performed by considering several combinations of snow grains size and shape, snowpack
330   stratification and layer density. The code evaluates the upward and downward fluxes for both direct and diffuse radiation in
each layer within the snowpack at wavelengths between 200 nm and 5 μm and the spectral albedo is finally derived from the
balance of upward and downward fluxes at the top interface (Briegleb et al., 2007). Differently from the common use of
calculating the spectral albedo, in this work we propose to exploit the power of SNICAR simulation algorithm to obtain precise
radiation fluxes as a function of depth into the snowpack at high resolution (about 1 mm). Introducing all the physical
335   information available about the snow measured on the field and by comparing numerical simulations to our probe data, this
approach allows us to roughly assess how sunlight propagates within the sampled snowpack. Finally, one can attempt to
extrapolate the behaviour of UV radiation through the snowpack, based upon the strong constraints given by the experimental
measurements.

We estimate the flux of light scattered in the horizontal direction to be proportional to the sum of the two vertical ones,
340   downward and upward. To approach the data analysis in a quite general way, we do not fit to data the parameters of some
simulation: we examine the results of a relatively huge number of simulations as follows. An extended set of results has been
obtained by running SNICAR code for a wide range of values of the main parameters defining the snowpack. We assumed
clean snow with different kind of grain shapes: spheroid, hexagonal plate and Koch fractal snowflakes (Dominé et al., 2003;
Erbe et al., 2003). We spanned grain sizes from 50 μm up to 1500 μm for each shape. The threshold value of 1500 μm was
345   selected as no larger snow grains were ever observed in any of the presented cases. Aspect ratios and shape factors for non-
spherical grains have been maintained as the default ones, as indicated by He et al. (2017). The spectral refractive index of
snow was taken from Picard et al. (2016). Finally, only the case of dry snow and clear sky conditions were accounted for,
being adequate to the specific conditions of all our measurements reported below. For each measurement, the simulations have
been performed for three values of the Solar Zenith Angle: ϑ_0, $\vartheta_0 \pm 2°$, where ϑ_0 is the real value obtained from the ephemeris
350   for the specific measurement. A very weak dependence of the results is actually emerging. We compare the SNICAR simulated
fluxes at 550 nm wavelength to data in the G band, for which an absolute calibration has been performed, and extract the input
parameters providing the light penetration profiles matching the data within a given discrepancy. The discrepancy, defined as
the sum of the normalized absolute differences (in %) between the measured and simulated curves, has been constrained within
10%. This "blind" approach has the strong advantage to automatically give information about the sensibility of the results
355   upon the input parameters, an issue that is of utmost importance to understand a) how much reliable is a description and b) the
actual importance of each parameter. The vertical normalization of the curves has been given as a free parameter.

2.5 Description of the snowpacks in the field experimental sites

The probe has been tested under different illumination conditions and with diverse snowpack characteristics. The measuring
sites were mainly selected in the western Italian Alps (Testa Grigia, Cime Bianche, Pt. Helbronner). Also, Arctic Spring

360 snowpack has been studied to cover a wider class of snow types: one site close to Ny-Ålesund Research Station (Svalbard archipelago, Norway) and one site on the Edithbreen glacier (Svalbard islands). In all the considered sites, the measurements have been performed on a snowpack of both freshly fallen and deposited, partially metamorphosed snow All measurements were performed in clear sky conditions between 10 am and 1 pm UTC. In Table 1 we list the main geographical characteristics of the measuring sites, including main snowpack conditions, orientation, coordinates and altitude, as well as the date and time

365 of the day and the Solar Zenith angle at which the measurements were performed.

	Site #1	**Site #2**	**Site #3**	**Site #4**	**Site #5**
Measuring site	Testa Grigia	Cime Bianche	Pt. Helbronner	Edithbreen glacier	Ny-Ålesund
Snow condition	Precipitation particles (PP), associated with RG, dry/moist	Artificial snow, dry	Melted forms, (MF) with dust (Saharan event), moist	Precipitation particles (PP) associated with SH and FC, dry	Rounded grains (RG), dry
Aspects	WSW	SE	SE	SW	NE
Coordinates	45° 56' N 7°42' E	45°54' N 7°40' E	45°50' N 6°56' E	78°51' N 12°8' E	78°55' N 11°55' E
Altitude [m]	3459	2866	3375	500	30
Date [dd/mm/yy]	24/01/23	28/01/23	08/07/23	10/04/22	24/03/23
Time [UTC]	12:51	10:00	10:00	10:00	10:39
ϑ_0 **[deg]**	77.9	68.2	30.6	70.8	77.6
Solar rad. flux [Wm^{-2}]	629.39	840.78	851.42	677.84	546.01

Table 1: main snowpack characteristics, orientation, geographical coordinates and altitude of the measuring sites; the date and time of the day and the Solar Zenith angle in which measurements were performed are also reported, thus allowing to retrieve information on solar radiation flux. The two sites in Svalbard archipelago were selected to have opposite geographical aspects (SW for Ny-

370 **Ålesund, NE for the Edithbreen glacier) to eventually evaluate the effects of different stratigraphical and compositional snow conditions. This was possible because during the indicated periods all slopes are properly illuminated by the Sun throughout the day.**

The solar radiation flux, expressed in watts per square meter (W m^{-2}), is also reported for each site in view of subsequent data
375 comparison. The solar flux was obtained using the open-source library Pysolar (https://github.com/pingswept/pysolar) by
knowing the geographical location of the measurement site and the time at which the sampling was done.

3 Results

In Fig. 5 we show typical profiles obtained through the upper part of snowpacks reported in Table 1. Red circles, green triangles
and blue squares represent the normalized radiation flux measured for the corresponding colour at the given depths, reported
380 in abscissas in units of mm. Data are normalized at z = 0 for each colour.

<table>
<tr><td>(a) site #1, Testa Grgia</td><td>(b) site #2, Cime Bianche</td><td>(c) site #3, Pt. Helbronner</td></tr>
<tr><td>(d) site #4, Edithbreen glacier</td><td>(e) site #5, Ny-Ålesund</td><td>(f) site #5, Ny-Ålesund</td></tr>
</table>
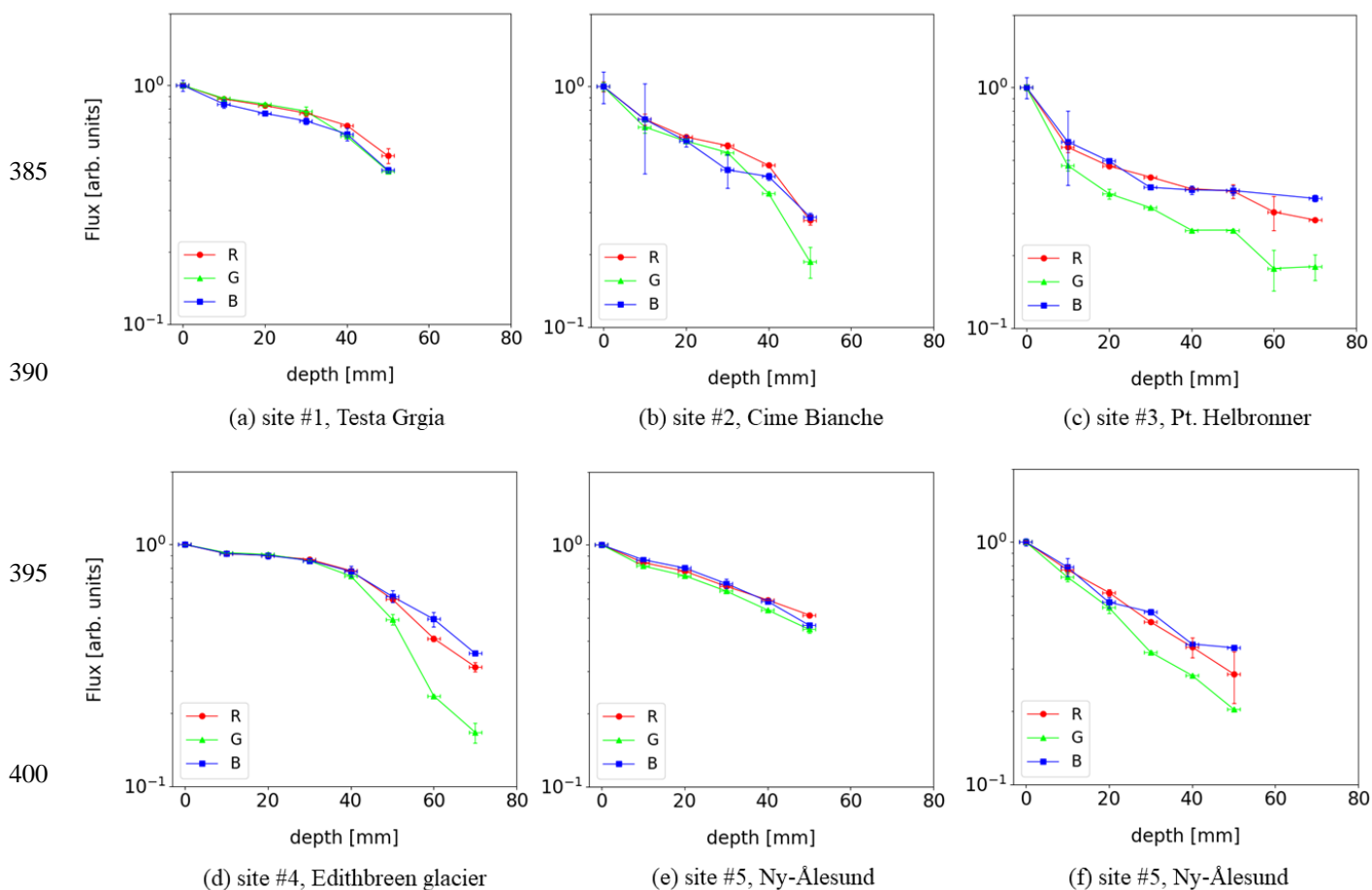
Figure 5: Experimental results. (a) site #1, Testa Grigia; (b) site #2, Cime Bianche (c) site #3, Pt. Helbronner; (d) site #4, Edithbreen
405 **glacier; (e) and (f) site #5, Ny-Ålesund, with two different snow densities (see Table 2 for further information), under peculiar**
conditions as described in the text. Abscissas are depths from the surface in mm, ordinates flux values normalized on the first

measurement at z=0, reported on a logarithmic scale. Horizontal uncertainty bars are estimated from the spatial resolution of the probe, while vertical bars correspond to the standard deviation of the ten measurements acquired for each depth value.

410 Data are plotted on a log-lin scale to better evidence whether the decay is exponential. Different behaviours are observed, from the pure exponential decay to a peculiar plateau followed by a steep knee. Evidence is there that different profiles show a clear dependence upon the snow type and conditions. Although this is clearly expected on a qualitative basis, we point out that our data give quantitative information with a relatively high spatial resolution. To exploit the SNICAR model and to compare numerical solutions to data, we carefully characterized the snow at each site in terms of grain size and snow density, ranging

415 from depth hoar and wind-packed (around 300 kg m^{-3}) to wet snow (typically around 600 kg m^{-3}), with a spatial resolution of 10 mm. Snow density was measured using a custom-made cutter; grain size was determined through nivological analyses by observing them on a crystallographic board through a lens with a 10x magnification. Since the uppermost layers of the snowpack resulted to be sufficiently homogenous, SNICAR model calculations were carried out by considering one average value for both snow density and grain size. Figures 5 (a) and 5 (b) are examples of the data obtained on the Italian Alps (site #1 and site #2 respectively) for two representative snowpacks composed by fresh snow and artificial snow, respectively. The

420 #1 and site #2 respectively) for two representative snowpacks composed by fresh snow and artificial snow, respectively. The exponential decay is evident, with small differences among the three-color bands that are outside the scope of this work. We point out that the exponential decay clearly indicates diffusive propagation: therefore, no preferential direction is imposed by the Solar Zenith angle ϑ_0 and the vertical coordinate z can be safely adopted as described by the equations presented above. Data shown in Fig. 5 (c) have been collected after a strong Saharan dust transport event in late spring 2023, so that the

425 uppermost layer presented a high concentration of impurities. The snowpack was then characterized by a high concentration of impurities, especially in the most superficial layer. Figure 5 (d) reports data obtained from pristine snow just deposited on top of the Edithbreen glacier in spring 2022. The last two panels (Fig. 5 (e−f)) report experimental results specifically obtained to check the system under peculiar illumination conditions with the snow very uniform and dry, thus easier to be modelled. A trench has been dug and the probe inserted into the wall along a direction corresponding (or very close) to the sunward

430 direction, just realizing the condition $\vartheta_0=0°$. The two measurements were performed with snow characterized by different densities (see Table 2 for further information) at 25 cm and 30 cm (Fig. 5 (e) and 5 (f), respectively), very uniform and dry in both cases, thus easy to be modelled.

Figure 6 shows the radiation fluxes measured in the G band and expressed in Wm^{-2} for each case reported separately in Fig. 5. These curves have been absolutely calibrated to further evidence the relative differences between light penetration in the

435 different cases, that will be quantitatively discussed in the following section.

440
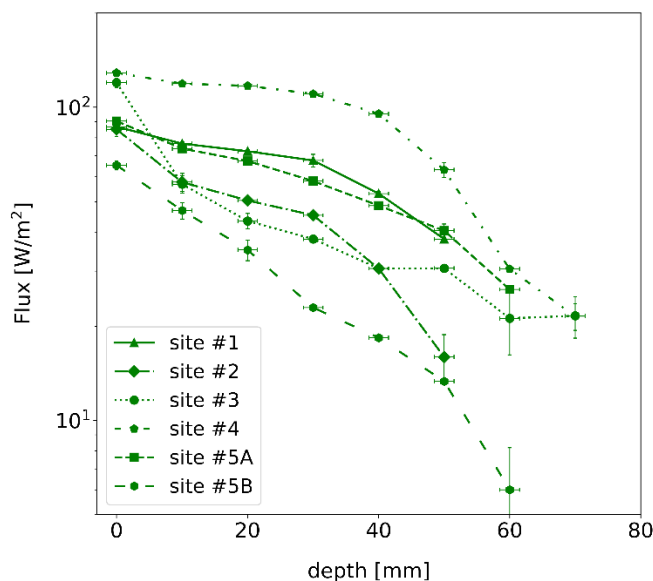
Figure 6: Radiation fluxes in the G band (ordinates in Wm^{-2}, log scale) at different depths below the snowpack surface (abscissas in mm). Uncertainties are reported as described above.

4 Discussion

Data show how snowpack properties clearly affect the characteristic length of sunlight penetration, characterized here by estimating the decay lengths as defined in Section 2.3. We estimate the decay length for the G band because the differences between the curves measured for the different spectral bands rather small. Different behaviours among R, G and B slopes are outside the scope of this work and deserve a specific treatment and investigation. Even more importantly, the absolute calibration has been performed for G band only (see Section 2.2). The absolute calibration is crucial when extrapolating to UV band, as we can predict the UV flux in Wm^{-2} as a function of depth (see Fig. A3 in Appendix B̶C). For site #1 and site #2 we obtain approximately $1/\gamma = 80$ mm and $1/\gamma = 40$ mm, both compatible with diffusive propagation (see for example Fig. 2.11 in Kokhanovsky, 2021). Moreover, they are in qualitative agreement with the behaviour expected from the different snow density measured on site (0.3 to 400 kg m^{-3} in site #1, above 650 kg m^{-3} in site #2), while the size of snow grains was approximately the same, around 0.1 mm in diameter (Kokhanovsky, 2021). The same applies for site #5A and site #5B, where density was in the order of 300 and 500 kg m^{-3} respectively and the grain size was still about 0.1 mm in diameter. Site #3 differs significantly from the previous ones, with a fast decrease in the upper 10-15 mm, followed by an exponential decay quite similar to what encountered before. This behaviour might be qualitatively explained by the strong absorption caused by the highly concentrated dust in the uppermost layer, that is outside the scope of the present work. Data from site #4 show a remarkable behaviour in the upper layer, where the decrease is much slower than in the previous cases: $1/\gamma > 200$ mm. By contrast, a steep decrease is evident below 50 mm, with a decay length of the order of $1/\gamma = 10\text{-}20$ mm, much smaller than above despite the

uniform snowpack. Although possible in principle, both values are incompatible with a purely diffusive propagation and a
non-diffusive process in the upper layers might be at the origin of this effect (Beaglehole et al., 1998).

475 These results clearly show a strong dependence of the characteristic propagation length, therefore of the actual extension of
the photic zone, on the peculiar properties of the snowpack.

4.1 Field data interpretation through the SNICAR simulations

Data collected in sites #1, #2 and #5A-B can be nicely described by considering a homogenous snowpack consisting of clean
snow grains with radii between 30 μm and 100 μm, accordingly to what measured for each sampling site. Furthermore, snow

480 density is described by values ranging between 300 and 800 kg m⁻³, again in good agreement with our measurements. In Fig.
7 we report the simulated fluxes that differ from experimental data within 10%, as explained above. The model snowpack is
retrieved by exploiting the parameters listed in Table 2.
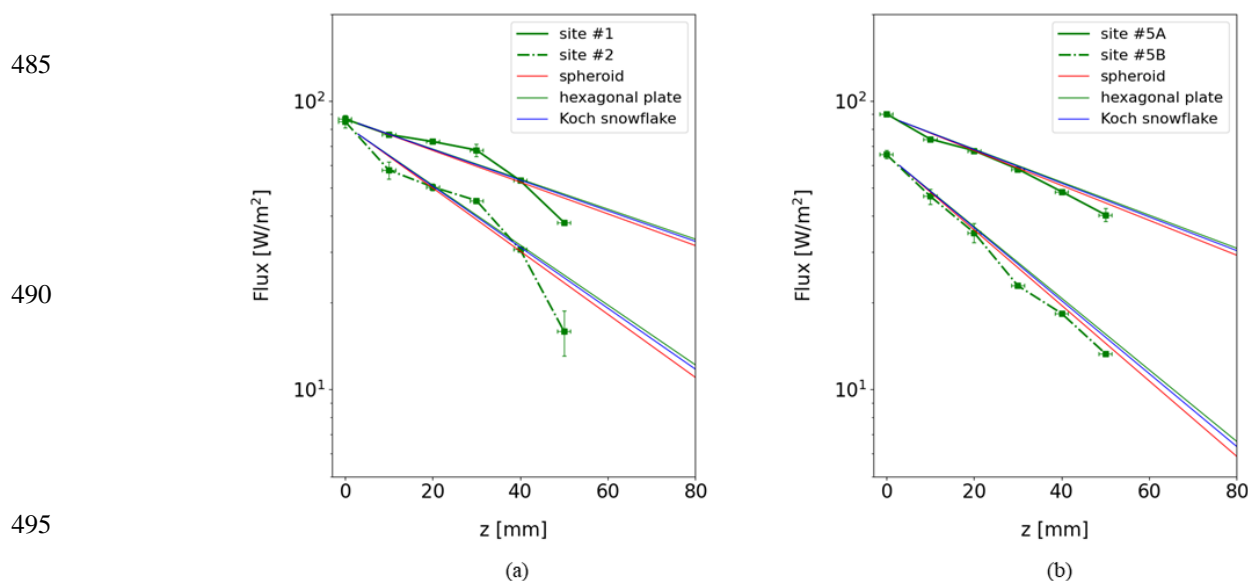
**Figure 7: Comparison of experimental results (represented in green) and vertical upward+downward light fluxes modelled through
SNICAR using homogeneous snowpacks composed of sub-millimetric clean snow grains: spheroids (red curves), hexagonal plates
(green curves) and Koch snowflakes (blue curves). Snowpack density ranges from 300 to 800 kg m⁻³, consistently with the**

500 **measurements on site. (a) site #1 and site #2; (b) site #5A and site #5B. Regarding uncertainties, the same applies as above.**

	Site #1	Site #2	Site #5A	Site #5B
Measuring site	Testa Grigia	Cime Bianche	Ny-Ålesund	Ny-Ålesund
Density [kg m^{-3}]	400 (300 to 400)	800 (>650)	300 (300 to 400)	500 (350 to 450)
Grain size [µm]	100 (50 to 200)	100 (50 to 200)	50 (50 to 100)	30 (20 to 60)
Grain shape	spheroid, hexagonal plate, Koch snowflake	spheroid, hexagonal plate, Koch snowflake	spheroid, hexagonal plate, Koch snowflake	spheroid, hexagonal plate, Koch snowflake

505

Table 2: Snowpack properties (layer density, grain size and shapes) retrieved by comparing the measured fluxes with the simulations at 550 nm wavelength. Both density and size agree with those obtained at sampling sites. Grain shape apparently has no significant effects in our measurements. Density and grain size values in round brackets represent the measured ones in each site.

510 Interestingly, we notice that grain shape is almost irrelevant in describing the propagation process of solar radiation within the snowpack: in all cases the layer density and grain radius provides a model that match the data irrespectively of the simulated geometries. We argue that this might be consistent with the measurements in the visible band, instead of infrared where typically the effect of snow grain structure is known to influence the propagation (actually, the albedo) (Dominé et al., 2006; Langlois et al., 2010).

515 The snowpack conditions at the Testa Grigia (site #1) and Ny-Ålesund (site #5A) were comparable with those of non-pristine, deposited and partially wind-packed snow. Thus, after metamorphism processes the snow grains presented a rounded morphology and small size without dendritic branches. On the other hand, as it is evident from Table 2, at the Cime Bianche site (#2) the comparison with the SNICAR simulation results yields an average snowpack density value of 800 kg m^{-3}, which is relatively high and more consistent with firn or basal ice than with snow. Actually, this value is compatible with the real

520 snowpack conditions, since the site was specifically selected to be close to the local ski resort where the artificial snow-making facilities were in operation, in order to investigate very peculiar conditions. It is well known that in the process of producing artificial snow, high-pressure water mist droplets are sprayed onto the slope, immediately freezing into cold air and resulting in small spheres of pure ice.

On the other hand, data collected in sites #3 and #4 cannot be explained within the frame of our simulations. In the case of

525 dusty snow (site #3), even by introducing the presence of dust at different concentrations the specific behavior cannot be reproduced. Even more remarkable is the difficulty in interpreting the data from pristine snow at site #4. The horizontally scattered light appears to be uniform across the first few tens of mm from the surface down, in strong disagreement with any

estimate for the scattering mean free path, expected to be a few mm maximum. Moreover, the abrupt transition to a fast decay is also still unexplained, showing the need of a more accurate study of this peculiar behavior.

530 **4.2 Simulated spectral albedo**

The SNICAR models fitting the data for sites #1, #2 and #5A-B allow us to extract the corresponding spectral albedo curves reported in Fig. 8. Although not directly measured, the curves are constrained by the high-resolution profiles measured with the probe.

Overall, the wavelength spectrum, small discrepancies are evident. They have been quantitatively estimated by averaging the
535 relative difference, computed as the normalized absolute differences (%) of each curve with respect to a reference one (site #1 in our case). Averages have been computed in the wavelength range 1-3 μm, which is the most affected by morphological properties of the snow grains. We point out that the complementary range <1 μm introduces negligible contribution (<0.2%), according to the minimum dependence on the snow structural and morphological properties in this interval. The relative differences for each site are listed in Table 3.
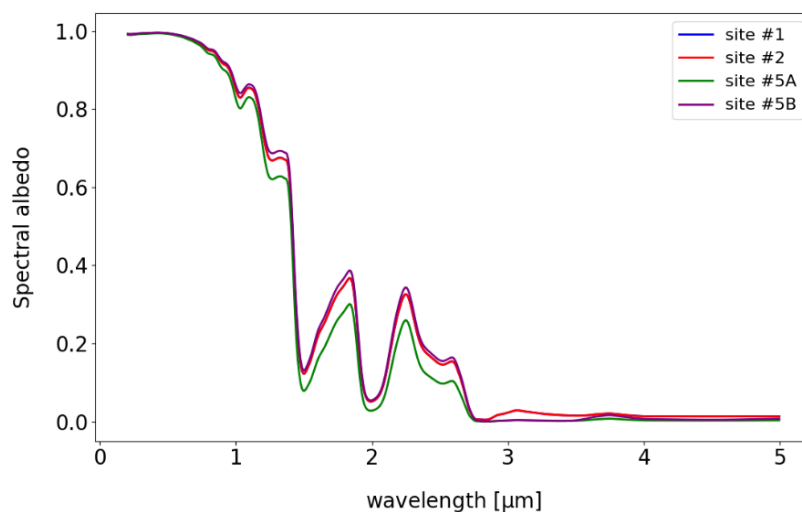
540

Figure 8: Modelled spectral albedo curves matching the experimental data for site #1, #2, #5A-B. Each curve is obtained as the arithmetic average of the three spectral albedo profiles retrieved through SNICAR model for each grain shape.

555

Measuring site	Relative discrepancy [%]
Cime Bianche (site #2)	0.03
Ny-Ålesund (site #5A)	30.34
Ny-Ålesund (site #5B)	12.67

560

Table 3: Relative differences of spectral albedo curves for sites #2, #5A-B with respect to the reference one (site #1), as defined in the text.

More precisely, by performing further analyses with our SNICAR simulation dataset, we find that the spectral albedo is
565 affected by grain size, while the flux behavior through the uppermost layers of the snowpack is mainly influenced by grain size and snow density. In both cases, the grain shape influence is negligible. The dependency on snow density evidences that one spectral albedo could originate from different features in the light propagation through the snowpack. As a reference, in Fig. 9 we report all the spectral albedo curves in our dataset matching the reference curve of site #1 (100 μm grain size) within a relative discrepancy of 10% and in Fig. 10 the corresponding total (upward+downward) sunlight flux propagating inside the
570 snowpack. Again, relative discrepancies have been computed in the wavelength range 1-3 μm.
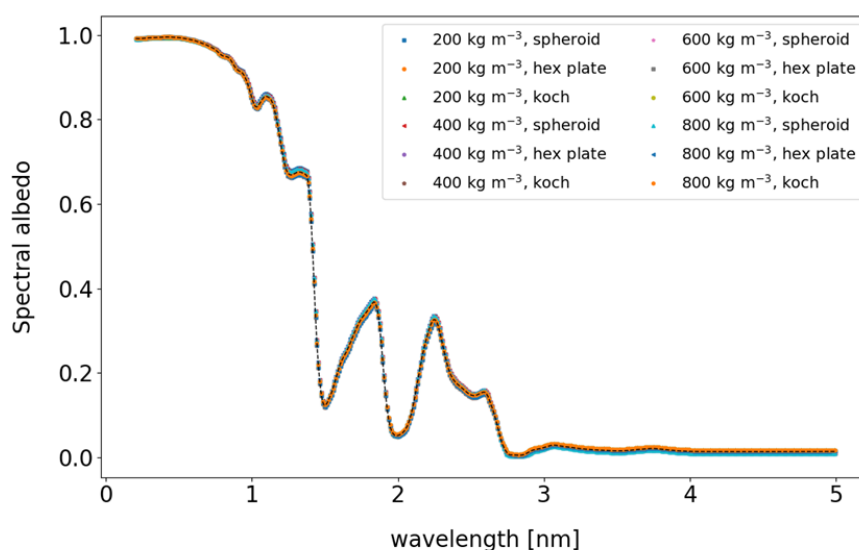
**Figure 9: Spectral albedo curves in our SNICAR dataset matching the reference curve of site #1 within a relative discrepancy of
585 10%.**
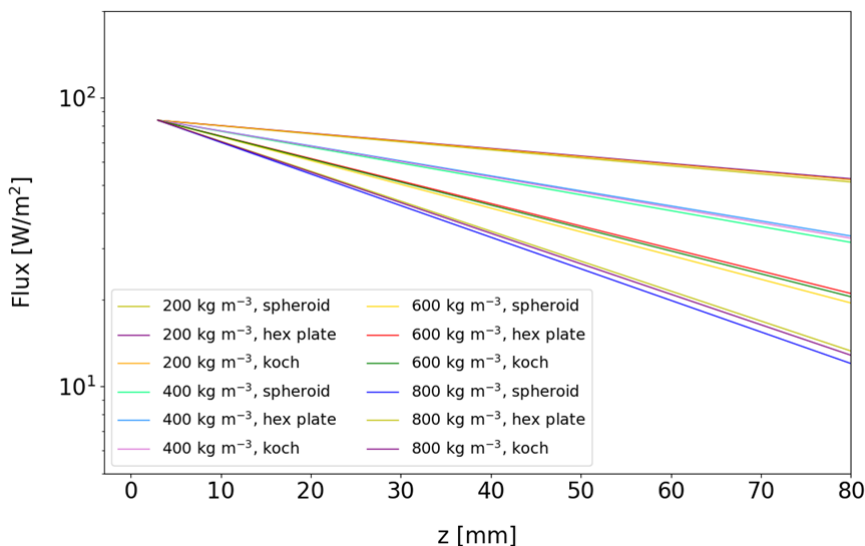
Figure 10: Total (upward+downward) sunlight flux propagating inside the snowpack corresponding to each spectral albedo profile in Fig. 9. The effect of different snow densities is evident.

The influence of different snow densities on the sunlight propagation through the snowpack is evident. In Table 4 we list the characteristic propagation lengths ($1/\gamma$) for the curves shown in Fig. 10. The very small variability in the slope of these curves is associated with the different possible snow crystal geometries.

Density [kg m^{-3}]	$1/\gamma$ [mm]
200	93 ÷ 95
400	66 ÷ 69
600	49 ÷ 52
800	34 ÷ 39

Table 4: Characteristic propagation lengths ($1/\gamma$) associated with different snowpack densities. In all cases, snow grains of 100 μm radius were considered, in agreement with the value derived from SNICAR comparison for site #1. Grain shape has a negligible impact, resulting in a variability of only a few millimetres.

We conclude that our measurements represent a piece of information that is complementary to the spectral albedo. It can be of importance when describing the light propagation through the snowpack in terms of snow grain morphology.

4.3 Extrapolating to the UV range

In the four cases where experimental data admit a clear numerical description, the possibility is open to extrapolate the same model snowpack and evaluate the UV radiation transfer and the UV fluxes at different depths. UV fluxes at a wavelength of 300 nm have been obtained through SNICAR from the same models discussed above. Results show that the slopes of the UV curves are systematically smaller than the VIS ones by about 25%. As expected, UV radiation penetrates deeper than visible light, extending the boundaries of the photic zone that is of interest for photochemical applications. Table 5 summarizes the results in terms of the characteristic propagation length ($1/\gamma$).

Measuring site	$1/\gamma$ [mm] - VIS	$1/\gamma$ [mm] - UV
Testa Grigia (site #1)	75.2 ± 0.4	105.1 ± 1.0
Cime Bianche (site #2)	40.6 ± 0.2	51.5 ± 0.7
Ny-Ålesund (site #5A)	66.7 ± 0.1	102.8 ± 0.7
Ny-Ålesund (site #5B)	37.4 ± 0.1	49.3 ± 0.4

Table 5: Characteristic propagation length ($1/\gamma$) retrieved from the comparison between the measured average flux in the VIS and UV region.

UV fluxes as a function of depth are reported in Fig. A3 (see Appendix B). Such information is recovered from the SNICAR output of the models matching the absolutely calibrated experimental data in the G band, thus making the extrapolation particularly robust and meaningful of the actual snowpack characteristics during the measurement.

5 Conclusions

We have developed and validated a robust and reliable probe to directly measure the sunlight propagation through the upper layers in all the type of snowpack. The probe has been realized to be lightweight and conveniently portable due to its compact design, while simultaneously being highly durable and stable. These features enable accurate and high-resolution measurements even in complex snowpack conditions characterized by different layers and melting-and-frost crusts formation.

635   The probe has been tested under different illumination conditions and with diverse snowpack characteristics, performing measurements in locations also characterized by different elevations. The results demonstrate that the characteristic propagation length (or e-folding depth), and therefore the actual extent of the photic zone, relies heavily on the unique attributes of the snowpack, as expected. We have shown that, besides the direct measurements, we can exploit the SNICAR code to find model snowpacks matching the probe data. For the cases that allow for an interpretation in terms of these numerical solutions,

640   the decay length is between 40 mm and 80 mm approximately. These values are compatible with diffusive sunlight propagation through the snowpack, as reported for example by Kokhanovsky (2021).

    By matching simulation results and data within the VIS spectrum, the model can be considered accurate enough to be extrapolated in the UV range of the sunlight, thus constituting a valid tool for estimating the UV flux within the snowpack, an issue that would pose important limitations from the point of view of the sensor and the UV radiation itself. The results show

645   an expected difference in slope between the UV and VIS profiles, with the UV curves consistently showing about a 25% reduction compared to the VIS ones. This suggests that, in these specific scenarios, UV radiation has the potential to penetrate slightly deeper than visible light, thereby extending the boundaries of the photic zone relevant for photochemical applications of few centimetres compared to the visible light.

    In perspective, this approach could be expanded to include the complementary information coming from the spectral albedo

650   measurements, thus introducing an additional constraint from completely independent measurements of the same snowpack. We point out anyway that the approach proposed here based upon experimental data about the light fluxes at different depths cannot be easily substituted by a similar process based upon fitting the snowpack model to data about the spectral albedo solely. As we have carefully checked, in many situations the same albedo curve can be explained by a set of different snowpack models, corresponding to diverse ways sunlight propagates through the snow. This degeneracy of the albedo curves for

655   different snowpacks and fluxes shows that some information is missing to correctly reproduce the radiative transfer in the real case. This also implies that extrapolation to the UV range will potentially fail.

    Extensive additional field measurements to compare with the corresponding simulations will be required to assess the contribution of non-ideal environmental conditions, such as cloudy sky, dusty layers or wet snow consequent of a Rain on Snow (RoS) event or during the melting.

660   In perspective, anyway, we foresee the potential advantage to operate both the measurements of the fluxes through the snowpack and the spectral albedo, that represent a complete set of experimental data that is possible to recover from such a complex system. Combining these measurements with a complete characterisation of the snowpack at high spatial resolution in terms of both snow density and grain size, as done in this work, would be of great relevance for future studies, especially in the case of non-homogeneous snowpacks.

665

Appendix A: Probe spurious effects

670

To assess the possible spurious effects introduced by the simple presence of the probe within the snowpack, the control system shown in Fig. A1 was designed. It consists of a cylindrical container 40 cm high and 20 cm in diameter. Test measurements were carried out by filling it with different types of materials (glass spheres of 2 mm in diameter, coarse salt and fine table salt), all of which were specifically selected to 'simulate' the diffusive propagation that can be found inside a snowpack. The

675   container was illuminated from above with a halogen lamp with a known spectrum and the 90° horizontally scattered radiation was measured through of an optical fiber coupled with a small glass prism (P), operated from underneath the container, thus not altering light propagation.

680

685

690
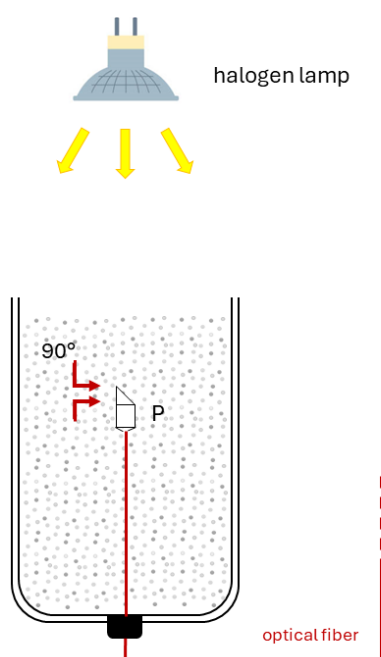
Figure A1: schematic of the validation procedure performed on analogue samples (see text for details). The light collection is obtained through a small glass prism (P) delivering the light collected at 90° through an optical fiber without affecting the light propagation

695   **(see the text for details).**

Measurements were performed with a calibrated power meter (Newport mod. 1815-C, Newport 818-SL) at wavelengths of 400, 500, 600, 700 and 800 nm using narrow-band spectral filters (model ThorLabs FKB-VIS-40, FWHM 40 nm). The comparison between these measurements and data collected operating the probe as we do in the snow are reported in Fig. A2.

700   Red, green and blue squares represent the normalized radiation flux measured with the probe for the corresponding colour at the given depths, reported in abscissas in units of mm. Again, data are normalized at z = 0 for each colour. Solid lines represent the normalized fluxes measured with the prism+optical fiber system for the corresponding spectral band.
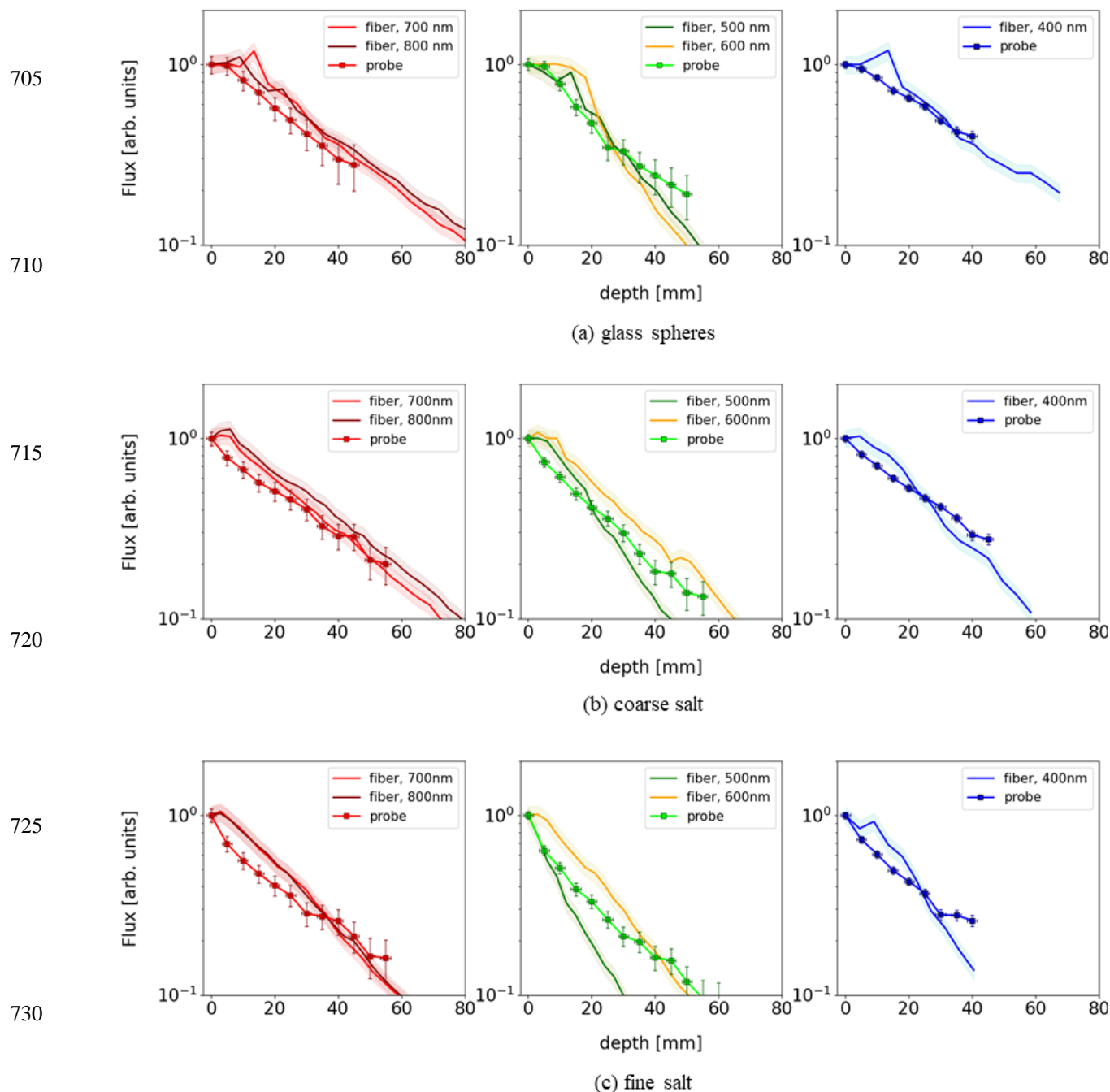
Figure A2: Experimental results. (a) glass spheres; (b) coarse table salt; (c) fine table salt. Abscissas are depths from the surface in mm, ordinates flux values normalized on the first measurement at z=0, reported on a logarithmic scale. Horizontal and vertical error bars related to probe measurements are reported as described above. Colour bands indicate the uncertainties associated with optical fiber measurements.

Appendix B: Extrapolating to the UV range

In Fig. A3 we report the UV fluxes at a wavelength of 300 nm as obtained from the same models reported in Fig. 7 and listed
740 in Table 2, an information that is directly present in the SNICAR output of the models matching the experimental data.
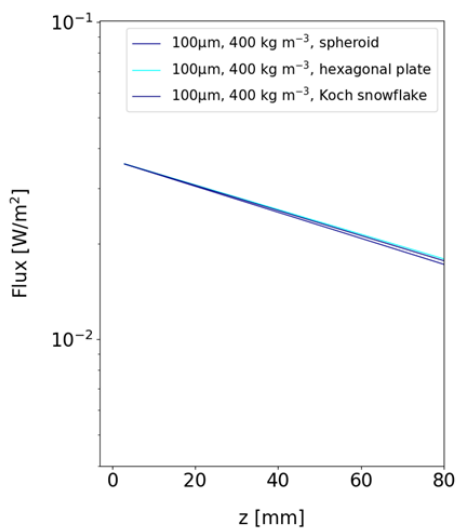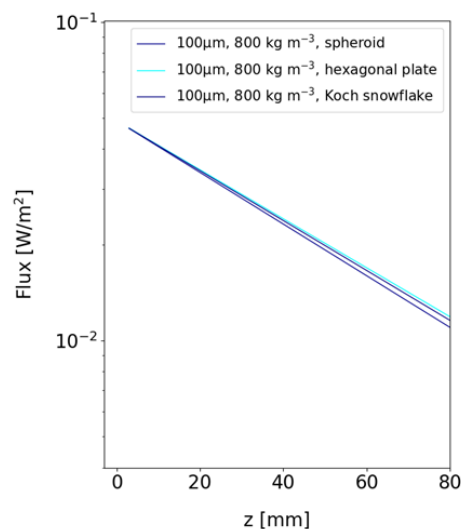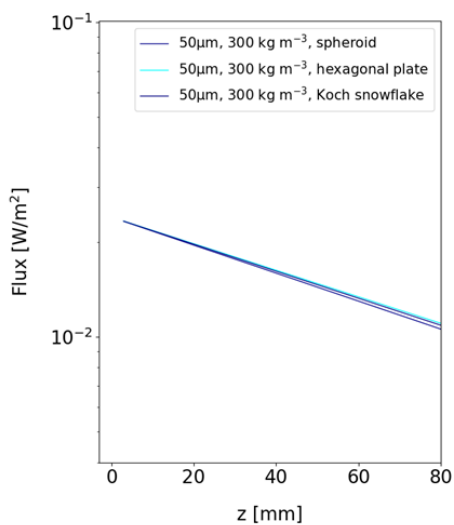
Figure A3: The fluxes of the total downward+upward UV radiation at 300 nm, obtained from the same SNICAR models matching the VIS data listed in Table 2. (a) site #1, Testa Grigia; (b) site #2, Cime Bianche; (c) site #5A, Ny-Ålesund; (d) site #5B, Ny-Ålesund.

770 Independently of the geometry considered for the snow grains, for each modelled snowpack the UV curves show a slope approximately 25% smaller than the corresponding VIS fluxes, which is consistent with the greater penetration expected for UV radiation than for visible light.

775 **Data availability.** This study used the SNICAR model version 3 code and database at https://github.com/mflanner/SNICARv3.

Author contribution

780 All authors contributed by conducting the field measurements, interpreting data and writing the manuscript. MP, LT, developed the methods, data analysis and interpretation. AS provided photochemical expertise. MP conceived the study and realized the probe. LT carried out the sensor calibration and performed SNICAR simulations.

785 **Competing interests**

The authors declare that they have no conflict of interest.

Acknowledgements. The author thanks Mark Flanner's team for making the SNICAR model publicly available
790 (https://github.com/mflanner/SNICARv3).

Financial support

This research received no financial support.

795

References

Beaglehole, D., Ramanathan, B., and Rumber, J.: The UV to IR transmittance of Antarctic snow, J. Geophys. Res. 103 (D8), 8849-8857, https://doi.org/10.1029/97JD03604, 1998.

Briegleb, B. P., and Light, B.: A Delta-Eddington multiple scattering parameterization for solar radiation in the sea ice component of the Community Climate System Model (No. NCAR/TN472+STR), National Center for Atmospheric Research, https://doi.org/10.5065/D6B27S71, 2007.

Cook, J. M., Tedstone, A. J., Williamson, C., McCutcheon, J., Hodson, A. J., Dayal, A., Skiles, M., Hofer, S., Bryant, R., McAree, O., McGonigle, A., Ryan, J., Anesio, A. M., Irvine-Fynn, T. D. L, Hubbard, A., Hanna, E., Flanner, M., Mayanna, S., Benning, L. G., van As, D., Yallop, M., McQuaid, J. B., Gribbin, T., and Tranter, M.: Glacier algae accelerate melt rates on the western Greenland Ice Sheet, The Cryosphere 14, 309–330, https://doi.org/10.5194/tc-14-309-2020, 2020.

Cooper, M. G., Smith, L. C., Rennermalm, A. K., Tedesco, M., Muthyala, R., Leidman, S. Z., Moustafa, S. E., and Fayne, J. V.: Spectral attenuation coefficients from measurements of light transmission in bare ice on the Greenland Ice Sheet, The Cryosphere 15, 1931–1953, https://doi.org/10.5194/tc-15-1931-2021, 2021.

Dang, C., Zender, C., Flanner, M. G.: Intercomparison and improvement of two-stream shortwave radiative transfer schemes in Earth system models for a unified treatment of cryospheric surfaces, The Cryosphere 13, 2325–2343, https://doi.org/10.5194/tc-13-2325-2019, 2019.

Dominé, F., Salvatori, R., Legagneux, L., Salzano, R., Fily, M., and Casacchia, R.: Correlation between the specific surface area and the short wave infrared (SWIR) reflectance of snow, Cold. Reg. Sci. Technol. 46, 60–68, https://doi.org/10.1016/j.coldregions.2006.06.002, 2006.

Dominé, F., Lauzier, T., Cabanes, A., Legagneux, L., Kuhs, W. F., Techmer, K., and Heinrich, T.: Snow metamorphism as revealed by scanning electron microscopy, Microsc. Res. Tech. 62, 33–48, https://doi.org/10.1002/jemt.10384, 2003.

Erbe, E. F., Rango, A., Foster, J., Josberger, E. G., Pooley, C., and Wergin, W. P.: Collecting, shipping, storing, and imaging snow crystals and ice grains with low-temperature scanning electron microscopy, Microsc. Res. Tech. 62, 19–32, https://doi.org/10.1002/jemt.10383, 2003.

Flanner, M. G., Zender, C. S., Randerson, J. T., and Rasch, P. J.: Present-day climate forcing and response from black carbon in snow, J. Geophys. Res. 112, D11202, https://doi.org/10.1029/2006JD008003, 2007.

Flanner, M. G., Arnheim, J. B., Cook, J. M., Dang, C., He, C., Huang, X., Singh, D., McKenzie Skiles, S., Chloe Whicker, C. A., and Zender, C. S.: SNICAR-ADv3: a community tool for modeling spectral snow albedo, Geosci. Model Dev. 14, 7673–7704, https://doi.org/10.5194/gmd-14-7673-2021, 2021.

Gerland, S., Liston, G.E., Winther, J.G., Ørbæk, J.B., and Ivanov, B.V.: Attenuation of solar radiation in Arctic snow: field
830 observations and modelling, Ann. Glaciol., 31, 364–368, https://doi.org/10.3189/172756400781820444, 2000.

Grannas, A. M., Jones, A. E., Dibb, J., Ammann, M., Anastasio, C., Beine, H. J., Bergin, M., Bottenheim, J., Boxe, C. S.,
Carver, G., Chen, G., Crawford, J. H., Dominè, F., Frey, M. M., Guzman, M. I., Heard, D. E., Helmig, D., Hoffmann, M. R.,
Honrath, R. E., Huey, L. G., Hutterli, M., Jacobi, H. W., Klan, P., Lefer, B., McConnell, J., Plane, J., Sander, R., Savarino, J.,
Shepson, P. B., Simpson, W. R., Sodeau, J. R., von Glasow, R., Weller, R., Wolff, E. W., and Zhu, T.: An overview on snow
835 photochemistry: evidence, mechanism and impacts, Atmos. Chem. Phys. Discuss. 7, 4165–4283, https://doi.org/10.5194/acp-
7-4329-2007, 2007.

Green, R. O., Dozier, J., Roberts, D., and Painter, T.: Spectral snow-reflectance models for grain-size and liquid-water fraction
in melting snow for the solar-reflected spectrum, Ann. Glaciol. 34, 71-73, https://doi.org/10.3189/172756402781817987,
2002.

840 Hamre, B., Winther, J. G., Gerland, S., Stamnes, J. J., and Stamnes, K.: Modeled and measured optical transmittance of snow-
covered first-year sea ice in Kongsfjorden, Svalbard, Geophys. Res 109, C10006, https://doi.org/doi:10.1029/2003JC001926,
2004.

He, C., Takano, Y., Liou, K.-N., Yang, P., Li, Q., and Chen, F.: Impact of Snow Grain Shape and Black Carbon-Snow Internal
Mixing on Snow Optical Properties: Parameterizations for Climate Models, J. Climate 30, 10019–10036,
845 https://doi.org/10.1175/JCLI-D-17-0300.1, 2017.

Jarvien, O., and Lepparanta, M.: Transmission of solar radiation through the snow cover on floating ice, J. Glaciol. 57(205),
861-870, https://doi.org/10.3189/002214311798043843, 2011.

Järvinen, O., and Leppäranta, M.: Solar radiation transfer in the surface snow layer in Dronning Maud Land, Antarctica, Polar
Science 7 1-17, https://doi.org/10.1016/j.polar.2013.03.002, 2013.

850 Kim, K., Kim, B., Ahn, Y.Y., Tran, K. D., Truong, H. T., and Kim, J.: Production of Molecular Iodine via a Redox Reaction
between Iodate and Organic Compounds in Ice, J. Phys. Chem. A 127, 12, 2830–2838,
https://doi.org/10.1021/acs.jpca.3c00482, 2023.

Kokhanovsy, A. A.: Snow Optics, Springer Nature Switzerland, 2021.

Kokhanovsky, A. A.: Light penetration in snow layers, J. Quant. Spectrosc. Radiat. Transf. 278, 108040,
855 https://doi.org/10.1016/j.jqsrt.2021.108040, 2022.

Lackner, G., Domine, F., Nadeau, D. F., Parent, A. C., Anctil, F., Lafaysse, M., and Dumont, M.: On the energy budget of a
low-Arctic snowpack, The Cryosphere 16, 127–142, https://doi.org/10.5194/tc-16-127-2022, 2022.

Langlois, A., Royer, A., Montpetit, B., Picard, G., Brucker, L., Arnaud, L., Harvey-Collard, P., Fily, M., and Goïta, K.: On the relationship between snow grain morphology and in-situ near infrared calibrated reflectance photographs, Cold. Reg. Sci.

860   Technol. 61, 34–42, https://doi.org/10.1016/j.coldregions.2010.01.004, 2010.

Libois, Q., Picard, G., France, J. L., Arnaud, L., Dumont, M., Carmagnola, C. M., and King, M. D.: Influence of grain shape on light penetration in snow, The Cryosphere 7, 1803–1818, https://doi.org/10.5194/tc-7-1803-2013, 2013.

Ma, X., Li, D., Fang, Y., Margulis, S. A., and Lettenmaier, D. P.: Estimating spatiotemporally continuous snow water equivalent from intermittent satellite observations: an evaluation using synthetic data, Hydrol. Earth Syst. Sci. 27, 21–38,

865   https://doi.org/10.5194/hess-27-21-2023, 2023.

Marks, A. A., and King, M. D.: The effect of snow/sea ice type on the response of albedo and light penetration depth (e-folding depth) to increasing black carbon, The Cryosphere 8, 1625–1638, https://doi.org/10.5194/tc-8-1625-2014, 2014.

Meirold-Mautner, I., and Lehning, M.: Measurements and model calculations of the solar shortwave fluxes in snow on Summit, Greenland, Ann. Glaciol. 38, 279-284, https://doi.org/10.3189/172756404781814753, 2004.

870   Mundy, C. J., Ehn, J. K., Barber, D. G. and Michel, C.: Influence of snow cover and algae on the spectral dependence of transmitted irradiance through Arctic landfast first-year sea ice, J. Geophys. Res. Oceans, 112, C03007, https://doi.org/10.1029/2006JC003683, 2007.

Obleitner, F.: The Energy Budget of Snow and Ice at Breidamerkurjökull, Vatnajökull, Iceland, Boundary-Layer Meteorol. 97, 385–410, https://doi.org/10.1023/A:1002734303353, 2000.

875   Pedersen, C. A., and Winther, J. G.: Intercomparison and validation of snow albedo parameterization schemes in climate models, Clim. Dyn 25, 351–362, https://doi.org/10.1007/s00382-005-0037-0, 2005.

Perovich, D. K.: Light reflection and transmission by a temperate snow cover, J. Glaciol. 53(181), 201-210, https://doi.org/10.3189/172756507782202919, 2007.

Picard, G., Libois, Q., and Arnaud, L.: Refinement of the ice absorption spectrum in the visible using radiance profile

880   measurements in Antarctic snow, The Cryosphere 10, 2655–2672, https://doi.org/10.5194/tc-10-2655-2016, 2016.

Raso, A. R. W., Custard, K. D., May, N. W., Tanner, D., Newburn, M. K., Walker, L., Moore, R. J., Huey, L. G., Alexander, L., Shepson, P. B., and Pratt, K. A.: Active molecular iodine photochemistry in the Arctic, PNAS 114 (38) 10053-10058, https://doi.org/10.1073/pnas.1702803114, 2017.

Robledano, A., Picard, G., Dumont, M., Flin, F., Arnaud, L., and Libois, Q.: Unraveling the optical shape of snow, Nat

885   Commun. 14, 3955, https://doi.org/10.1038/s41467-023-39671-3, 2023.

Robson, T. M., and Aphalo, P. J.: Transmission of ultraviolet, visible and near-infrared solar radiation to plant within a seasonal snowpack, Photochem. Photobiol. Sci. 18, 1963-1971, https://doi.org/10.1039/c9pp00197b, 2019.

Schlumpf, M., Hendrikx, J., Stormont, J., and Webb, R.: Quantifying short-term changes in snow strength due to increasing liquid water content above hydraulic barriers, Cold Reg. Sci. Technol. 218 104056, https://doi.org/10.1016/j.coldregions.2023.104056, 2024.

Seidel, K., and Martinec, J.: Remote Sensing in Snow Hydrology, Springer Berlin, Heidelberg, https://link.springer.com/book/9783540408802, 2011.

Spolaor, A., Angot, H., Roman, M., Dommerergue, A., Scarchilli, C., Vardè, M., Del Guasta, M., Pedeli, X., Varin, C., Sprovieri, F., Magand, O., Legrand, M., Barbante, C., and Cairns, W.R.L.: Feedback mechanisms between snow and atmospheric mercury: Results and observations from field campaigns on the Antarctic plateau, Chemosphere 197, 306-317, https://doi.org/10.1016/j.chemosphere.2017.12.180, 2018.

Spolaor, A., Barbaro, E., Cappelletti, D., Turetta, C., Mazzola, M., Giardi, F., Björkman, M. P., Lucchetta, F., Dallo, F., Pfaffhuber, K. A., Angot, H., Dommergue, A., Maturilli, M., Saiz-Lopez, A., Barbante, C., and Cairns, W. R. L.: Diurnal cycle of iodine, bromine, and mercury concentrations in Svalbard surface snow, Atmos. Chem. Phys. 19, 13325–13339, https://doi.org/10.5194/acp-19-13325-2019, 2019.

Tuzet, F., Dumont, M., Arnaud, L., Voisin, D., Lamare, M., Larue, F., Revuelto, J., and Picard, G.: Influence of light-absorbing particles on snow spectral irradiance profiles, The Cryosphere 13, 2169–2187, https://doi.org/10.5194/tc-13-2169-2019, 2019.

Varsa, P. M., Baranoski, G. V.G., and Kimmel, B. W.: SPLITSnow: A spectral light transport model for snow, Remote Sens. Environ. 255, 112272, https://doi.org/10.1016/j.rse.2020.112272, 2021.

Vérin, G., Domine, F., Babin, M., Picard, G and Arnaud, L.: Metamorphism of snow on Arctic sea ice during the melt season: impact on spectral albedo and radiative fluxes through snow, The Cryosphere 16, 3431–3449, https://doi.org/10.5194/tc-16-3431-2022, 2022.

Warren, S. G., Brandt, R. E., and Grenfell, T. C.: Visible and near-ultraviolet absorption spectrum of ice from transmission of solar radiation into snow, Appl. Opt. 45(21), 5320-5334, https://doi.org/10.1364/ao.45.005320, 2006.

Whicker, C. A., Flanner, M. G., Dang, C., Zender, C. S., Cook, J. M., and Gardner, A. S.: SNICAR-ADv4: a physically based radiative transfer model to represent the spectral albedo of glacier ice, The Cryosphere 16, 1197–1220, https://doi.org/10.5194/tc-16-1197-2022, 2022.

Zhou, X., Li, S., and Stamnes, K.: Effects of vertical inhomogeneity on snow spectral albedo and its implication for optical remote sensing of snow, J. Geophys. 108 (D23), 4738, https://doi.org/10.1029/2003JD003859, 2003.